The Role of Ridges in the Formation and Longevity of Flat Slabs

SANJA KNEZEVIC ANTONIJEVIC[1*], LARA S. WAGNER[2], ABHASH KUMAR[1], SUSAN L. BECK[3], MAUREEN D. LONG[4], GEORGE ZANDT[3], HERNANDO TAVERA[5], CRISTOBAL CONDORI[5]

[1] Department of Geological Sciences, University of North Carolina at Chapel Hill, CB #3315, Chapel Hill, North Carolina, 27599, USA

[2] Department of Terrestrial Magnetism, Carnegie Institution for Science, 5241 Broad Branch Road, NW, Washington, DC, 20015, USA

[3]Department of Geosciences, University of Arizona, 1040 E. 4th St., Tucson, AZ 85721, USA

[4]Department of Geology and Geophysics, Yale University, 210 Whitney Ave., New Haven, Connecticut, 06511

[5]Instituto Geofísico del Perú, Calle Badajoz #169, Lima, Perú

*e-mail: sknezevi@live.unc.edu

The Role of Ridges in the Formation and Longevity of Flat Slabs

ABSTRACT

Flat slab subduction is often proposed as a mechanism for the genesis of thick-skinned crustal deformation far from plate boundaries and unusual patterns of volcanism dating as far back as the Proterozoic[1]. For example, the formation of the expansive Rocky Mountains and the subsequent voluminous volcanism across much of the western United States has been attributed to a broad region of flat subduction beneath North America during the Laramide Orogeny (80-55 Ma)[2]. Here we study the largest modern flat slab, located in Peru, to better understand the processes controlling the formation and along-strike extent of flat slabs. We present new data that indicate the subducting Nazca Ridge is necessary for the development and continued support of the horizontal plate at ~90 km depth. By combining constraints from Rayleigh wave phase velocities with improved earthquake locations, we find that the flat slab is shallowest along the ridge, while to the northwest of the ridge, the slab is sagging, tearing, and re-initiating normal subduction. Based on our observations, we propose a conceptual model for the temporal evolution of the Peruvian flat slab in which the flat slab forms due to the combined effects of trench retreat, suction, and ridge subduction. We find that while the ridge is necessary but not sufficient for the formation of the flat slab, its removal is sufficient for the flat slab to fail. This provides new constraints on the processes controlling the beginning and end of the Laramide Orogeny and other putative episodes of flat slab subduction.

Flat slabs represent the horizontal end-member of the range of dip angles observed in subducting oceanic plates. The subduction of buoyant aseismic ridges and plateaus comprising over-thickened oceanic crust has long been thought to play a role in the formation of flat slabs[3]. More recent work has identified other potential contributing factors including trench retreat[4,5], rapid overriding plate motion[4,5], and suction between the flat slab and overriding continental mantle lithosphere[5]. Many of these studies do not preclude the need for additional buoyancy from over-thickened oceanic crust. However, a few recent studies suggest that subducting ridges do not play any role in the formation or sustainability of flat slabs [6,7].

In order to evaluate the influence of subducting ridges on the evolution of flat slabs, we focus on the flat slab in southern Peru (Fig. 1). Here, the subducting Nazca Ridge trends at an oblique angle to relative plate motion, resulting in a northward migration of the overriding continent relative to the downgoing ridge[8]. We have collected and analyzed data from two recent deployments of broadband seismometers in central and southern Peru: PULSE (PerU Lithosphere and Slab Experiment)[9], and CAUGHT (Central Andean Uplift and Geodynamics of High Topography)[10]. We also incorporate data from 8 stations from the PERUSE deployment (Peru Slab Experiment)[11] and the permanent station NNA in Lima, Peru (Fig. 1). Here we present a 3D model of shear wave velocity structure between 10°S and 18°S obtained from the inversion of earthquake-generated Rayleigh wave phase velocities (Fig. 2, Fig. S2-10). We also relocate slab seismicity across our study area using a double difference methodology (Fig. 2 and 3, Fig. S1, Table S1) (see Methods for details).

Our tomographic images and improved earthquake relocations show the flat slab to be shallowest along the present-day projected location of the subducted Nazca Ridge (Fig. 2g, 3g, h). To the south (Fig. 2h), the slab transitions abruptly from flat to normal, and earthquake locations align with an observed high shear wave velocity anomaly. To the north, where previous studies have proposed a broad flat slab of relatively uniform depth[13,14], we see a gradual but marked deepening of the Wadati-Benioff zone (Fig. 2e-f, 3g-h). To the east, high shear wave velocities associated with the flat slab extend significantly further inboard than the seismically active portion of the plate (Fig. 2g, 3g-h). The downward bend in the high velocity plate at the inboard extent of the flat slab appears to coincide with the location of the trench at ~10 Ma[8].

Of particular note is the geometry of the subducted plate north of the projected Nazca Ridge track (Fig. 2 a, b, c, e, f). Here, we observe a dipping high velocity anomaly trenchward of a dipping low velocity anomaly. We note the similarity between these structures (in an area previously believed to comprise typical flat slab) and those observed to the south beneath the active arc (Fig. 2e-f ; Fig 2h). We also note the difference between these structures from those observed adjacent to the ridge, where the continuous flat slab is well resolved (Fig. 2e-f; Fig 2g; Supplemental Fig. 3,6-10). We interpret the westward-dipping trench-parallel low velocity region to be evidence of asthenosphere between two torn portions of subducted plate. The dipping high velocity anomaly to the west indicates the presence of a normally dipping slab extending to at least 200 km depth. This is consistent with the location of scatterers identified in earlier studies of ScSp phases[15]. We propose that the subhorizontal seismicity to the east of the tear is located in remnant flat slab that has not yet been fully subducted. Local shear wave splitting studies show trench parallel fast directions[9], consistent with north-south directed asthenospheric flow through a break in the Nazca plate. We also note the presence of a localized high heat flow measurement above this low velocity anomaly (196mW/s²)[16] (Fig. 2e). Along the northernmost transect the location of the slab is not well resolved above ~100 km depth (Fig. 2e). Future work using ambient noise tomography may help us resolve the slab geometry here by providing improved constraints on velocities at shallower depths.

We incorporate the results of previous geodynamic modeling studies to create a conceptual model of the temporal evolution of the Peruvian flat slab (Fig. 3). We begin with the initiation of ridge subduction at ~11.2 Ma[8], prior to which we assume normal subduction across our study area (Fig. 3a). From there, we base our proposed temporal evolution of the Peruvian flat slab on four principles. First, we present our conceptual model from the reference frame of a laterally stationary Nazca plate. Second, while most of the Nazca plate sinks vertically at a relatively constant rate, the plate containing the Nazca Ridge ceases to sink at ~90 km depth (Fig. 3b-f). We propose that this is due to buoyancy imparted by the overthickened oceanic crust and harzburgite layer associated with the ridge, consistent with previous modeling studies[17]. The third principle controls the inboard extent of the flat slab. We observe that the modern inboard extent of the Peruvian flat slab corresponds to the location of the trench at ~10 Ma. Given that the projected Nazca Ridge location extends further to the east, this suggests that some portion of the Nazca Ridge has resumed normal subduction. We propose that over time, the kinetically slow eclogitization of the over-thickened crust of the Nazca Ridge results in an increase in density of the horizontal plate. Based on the inboard extent of the modern flat slab, we propose that approximately 10 Ma after entering the trench, the over-thickened oceanic crust of the Nazca Ridge becomes sufficiently eclogitized that it is no longer neutrally buoyant and therefore resumes its vertical descent (Fig. 2b,g, 3e-g).

Finally, modeling studies indicate that suction between the horizontal plate and overriding continental lithosphere hinders the removal of the flat slab[5]. In our study area, this is important because the portion of the continent under which the flat slab initially forms moves northwest relative to the ridge over time. To test if the flat slab will perpetuate beneath these continental regions after the departure of the ridge, we apply the fourth principle: continental regions previously underlain by the flat slab will continue to have flat slab beneath them for some time (brown regions, Fig. 3). This results in a broadening of the flat slab as new continental areas to the south become underlain by the ridge and associated flat slab, while areas to the north that were previously underlain by the ridge maintain their flat slab geometry. This is consistent with earlier studies that attribute the along-strike extent of the Peruvian flat slab to the southward sweep of the Nazca Ridge over time[8,9].

The proposed temporal evolution of the Peruvian flat slab shown in Figure 3 combines the influences of trench retreat/overriding plate motion, suction, and ridge buoyancy. It assumes that the combination of all three forces is necessary for the formation of the flat slab, but that the first two are sufficient to perpetuate the flat slab after the departure of the ridge. A comparison between our conceptual model's slab geometry at present (Fig. 3g) with actual (observed) slab geometry (Fig. 3h) allows us to test these assumptions. The abrupt edge of the flat slab that we observe south of the ridge is very similar to that proposed by our conceptual model. We note that the dominant model principle controlling the geometry of the flat slab here is the effect of ridge buoyancy, as there is no difference in trench rollback or continental lithospheric structure that might affect suction along strike in this region. Our observations therefore support the necessary contribution of the ridge to the formation of flat slabs, but are also not inconsistent with additional contributions from suction and trench rollback.

Differences between our observed slab geometry and the geometry derived from our conceptual model are visible to the north of the ridge. In this area, the effect of the ridge is no longer present, and the geometry of the flat slab in our conceptual model is controlled by the effects of suction and trench rollback alone. While both our conceptual model and our observations indicate a flat slab that broadens to the northwest of the ridge, the detailed morphologies are very different. In addition to an overall deepening of the flat slab north of the ridge (Fig. 3g,h, Fig. S1), we observe a clear trench parallel break in the subducted plate and a resumption of normal subduction trenchward of this tear (Fig. 2a-c, 3h). This strongly suggests that, in spite of the presence of suction and trench rollback, the flat slab is no longer stable once the buoyant Nazca Ridge has been removed. Furthermore, once a break is present, the newly subducted plate assumes a normal steep dip angle, rather than a flat slab geometry. This study is not able to resolve the northern extent of the Peruvian flat slab, nor can we establish the along-strike extent of the tear. However, ISC catalog locations north of our study area show a gap in seismicity that may be consistent with the absence of a flat slab due to a progressively tearing plate (Fig. 3h)[19]. The northward extent of the flat slab east of the tear may be due in part to the subduction of the Inca Plateau[8], though this is beyond the scope of the present study.

Our model is applicable to all flat slab geometries where a distinct change of dip angle is observed. This change in dip occurs at the depth at which the slab becomes neutrally buoyant. Our results may not be applicable to slabs where the dip angle is constant but very shallow[7] (e.g. Alaska, Cascadia). Shallowly dipping slabs sink at a constant rate, which is inconsistent with a period of neutral buoyancy. Shallowly dipping slabs may have some similar consequences as flat slabs, though notably they do not result in a complete cessation of arc volcanism (as occurred during the Laramide and is observed in Peru today), only its inboard deflection.

Our results may provide important insights into the final stages of flat slab subduction. Previous studies use volcanic patterns to reconstruct the formation and foundering of the Farallon flat slab [2,20,21]. The diversity of models for the progression of this foundering is indicative of the insufficiency of the constraints provided by volcanic trends alone. Our results suggest that once the flat slab extends some distance away from the buoyant feature, it will begin to sink and/or tear. The tearing of the Farallon plate due to excessive flat slab width may be consistent with tomographic images of broken fragments of the Farallon plate[22].

We conclude that flat slabs form due to a combination of trench retreat, suction, and the inability of over-thickened oceanic crust to sink below some depth (~90 km) until sufficiently eclogitized to once again become negatively buoyant. Flat slabs that extend laterally beyond some critical distance from the buoyant over-thickened crust will begin to founder, even in the presence of other factors such as suction and trench retreat. The Peruvian flat slab provides insights into the temporal evolution of flat slabs from initial shallowing to collapse, yielding new constraints for the reconstruction of flat slab genesis and the nature of the flat slab foundering.

REFERENCES

1. Bedle, H., & van der Lee, S. Fossil flat-slab subduction beneath the Illinois basin, USA. *Tectonophysics*, ***424***(1), 53-68 (2006).
2. Humphreys, E., Hessler, E., Dueker, K., Farmer, G. L., Erslev, E., & Atwater, T. How Laramide-age hydration of North American lithosphere by the Farallon slab controlled subsequent activity in the western United States. *Int. Geol. Rev*. **45**(7), 575-595 (2003).
3. Vogt, P. R.. Subduction and aseismic ridges. *Nature,* **241**, 189-191 (1973).
4. van Hunen, J., Van Den Berg, A. P., & Vlaar, N. J. On the role of subducting oceanic plateaus in the development of shallow flat subduction. *Tectonophysics* **352**(3), 317-333 (2002).
5. Manea, V. C., Pérez-Gussinyé, M., & Manea, M. Chilean flat slab subduction controlled by overriding plate thickness and trench rollback. *Geology* **40**(1), 35-38 (2012).
6. Gerya, T. V., Fossati, D., Cantieni, C., & Seward, D. Dynamic effects of aseismic ridge subduction: numerical modelling. *Eur. J. Mineral*. **21**(3), 649-661 (2009).
7. Skinner, S. M., & Clayton, R. W. The lack of correlation between flat slabs and bathymetric impactors in South America. *Earth and Planet. Sci. Lett*. **371**, 1-5 (2013).

8. Rosenbaum, G., Giles, D., Saxon, M., Betts, P. G., Weinberg, R. F., & Duboz, C. Subduction of the Nazca Ridge and the Inca Plateau: Insights into the formation of ore deposits in Peru. *Earth and Planet. Sci. Lett*. **239**(1), 18-32 (2005).

9. Eakin, C. M., Long, M. D., Beck, S. L., Wagner, L.S., Tavera, H. & Condori, C. (2014). Response of the mantle to flat slab evolution: Insights from local S splitting beneath Peru. *J. Geophys. Res*. **41**(10), 3438-3446 (2014).

10. Ward, K. M., Porter, R. C., Zandt, G., Beck, S. L., Wagner, L. S., Minaya, E., & Tavera, H. Ambient noise tomography across the Central Andes. *Geophys. J. Int.* **194**(3), 1559-1573 (2013).

11. Phillips, K., & Clayton, R. W. Structure of the subduction transition region from seismic array data in southern Peru. *Geophys. J. Int*. ggt504 (2014).

12. Gripp, A. E., & Gordon, R. G. Young tracks of hotspots and current plate velocities. *GJI.* **150**(2), 321-361 (2002).

13. Cahill, T., & Isacks, B. L. Seismicity and shape of the subducted Nazca plate. *J. Geophys. Res*: *Solid Earth.* (1978–2012), **97**(B12), 17503-17529 (1992).

14. Hayes, G. P., Wald, D. J., & Johnson, R. L. Slab 1.0: A three-dimensional model of global subduction zone geometries. *J. Geophys. Res*.: *Solid Earth.* (1978–2012), **117**(B1) (2012).

15. Hasegawa, A., & Sacks, I. S. Subduction of the Nazca plate beneath Peru as determined from seismic observations. *J. Geophys. Res*.: *Solid Earth.* (1978–2012), **6**(B6), 4971-4980 (1981).

16. Uyeda, S., Watanabe, T., Ozasayama, Y., & Ibaragi, K. Report of heat flow measurements in Peru and Ecuador. *Bull. Of the Earthquake Res. Institute* **55**, 55-74 (1980).

17. Arrial, P. A., & Billen, M. I. Influence of geometry and eclogitization on oceanic plateau subduction. *EPSL***,** **363**, 34-43 (2013).

18. Instituto Geológico Minero y Metalúrgico – INGEMMET, On-line Catalog, http://www.ingemmet.gob.pe, Peru (2014).

19. International Seismological Centre, *On-line Bulletin*, http://www.isc.ac.uk, Internatl. Seis. Cent., Thatcham, United Kingdom (2012).

20. Liu, L., Gurnis, M., Seton, M., Saleeby, J., Müller, R. D., & Jackson, J. M. The role of oceanic plateau subduction in the Laramide orogeny. *Nature Geoscience*, **3**(5), 353-357 (2010).

21. Jones, C. H., Farmer, G. L., Sageman, B., & Zhong, S. Hydrodynamic mechanism for the Laramide orogeny. *Geosphere*, ***7***(1), 183-201 (2011).

22. Sigloch, K., McQuarrie, N., & Nolet, G. Two-stage subduction history under North America inferred from multiple-frequency tomography. *Nature Geoscience*, **1**(7), 458-462 (2008).

Supplemental information is linked to the online version of the paper at www.nature.com/nature.

ACKNOWLEDGMENTS: We thank to Robert Clayton and Paul Davies for providing the records from 8 PERUSE stations. The PULSE experiment was supported by NSF grants EAR-0944184 (LSW), EAR-0943991 (SLB), EAR-0943962 (MDL). The

CAUGHT project was supported by NSF grants EAR-0908777 (LSW) and EAR-0907880 (SLB).

AUTHOR CONTRIBUTIONS S.K.A. generated the tomographic model. L.S.W. developed the model of temporal evolution. A.K. provided the earthquake locations. S.K.A, L.S.W., A.K. developed the ideas and wrote the paper. S.L.B., M.D.L., G. Z., H.T. and C.C. contributed to the data collection and paper editing.

AUTHOR INFORMATON Reprints and permission information is available online at http://npg.nature.com/reprintsandpermissions. Correspondence and requests for materials should be addressed to S.K.A.

Figure 1 | Reference map of the Peruvian flat slab region illustrating the subducting Nazca Ridge beneath the advancing South American plate. Diamonds represent stations used in this study: orange are PULSE, dark red are CAUGHT, yellow are PERUSE, and red is the permanent NNA station. Yellow stars represent cities Lima and Cusco. Red triangles are Holocene volcanoes. The black arrow indicates the relative motion of the South American plate with respect to the Nazca plate[12]. Dotted white lines show the estimated position of the Nazca Ridge ~11 Ma and today[8].

Figure 2 | Shear wave velocities and seismicity at 75, 105, and 145 km depth and transects along the northern re-initiating steep slab (A-A', B-B'), flat slab (C-C') and southern steep slab segments (D-D'). Colors indicate velocity deviations dVs/Vs (%), contours show absolute velocities. (**a**), (**b**), (**c**) Black circles represent stations used in the study; red triangles are Holocene volcanoes; green stars are earthquakes within 20 km of the depth shown; black lines refer to cross-sections shown in (**e**), (**f**), (**g**), and (**h**). The grey dashed line refers to the location of the trench 10 Ma[8]. The black dashed line ("T") in (**b**) and (**c**) indicates the location of the slab tear; R refers to the resumption of steep subduction at the eastern edge of the flat slab. (**d**) The inferred flat slab geometry along the Nazca Ridge track and slab tear north of the ridge. (**e-h**) Black dots show earthquake locations from this study, black inverted triangles are stations, red triangles are Holocene volcanoes, and the orange triangle represents the location of an unusually high heat flow measurement[16]. Dashed lines show the inferred top of the slab. The crustal thickness is shown with a thick black line in each cross-section.

Figure 3 | Proposed evolution of the Peruvian Flat Slab. Panels **a-f** show proposed contours of the subducted slab, assuming that the ridge remains buoyant for 10 Ma after entering the trench. The approximate location of the subducted ridge is denoted by the black rectangular outline. Brown areas show areas of the continent underlain by flat slab at each time step. Triangles indicate volcanoes active during the 2 Ma following the time of the frame shown[18]. The location of the South American continent relative to the Nazca Ridge follows Rosenbaum et al., (2005)[8]. In panel **a**) we show the proposed reflected location of the conjugate to the Nazca Ridge in yellow[8]. In panel **e**) red triangles show volcanism from 3-2 Ma, and brown triangles show volcanism for 2-1 Ma. In panel **f**) volcanism is shown for 1 to 0 Ma (not including Holocene volcanism). Panel **g**) shows modern seismicity from the present study with depths >50 km, and contours as they would be if the removal of the ridge did not affect the longevity of the flat slab. Panel **h**) shows modern seismicity from this study and local seismicity > 50 km depth as reported in ISC catalog for years 2004 – 2014 as smaller circles[19]. We plot our observed slab contours based on our earthquake locations and the location of high velocity anomalies in our tomographic results. Dashed lines indicate contours that are less certain due to either a paucity of seismicity or because they lie outside of our region of good tomographic resolution. The pink triangular shape shows the region with very limited seismicity that may indicate a slab window caused by tearing and the re-initiation of normal subduction.

METHODS

Earthquake locations

We use ANTELOPE software to auto-detect earthquakes, using a short term average (STA) versus long term average (LTA) trigger mechanism. The lengths of the STA and LTA moving time windows were chosen to be 1 second and 10 seconds respectively. After manually inspecting the waveforms, we selected 977 earthquakes out of 3000 auto-detected events. We picked P and S wave arrival times for 673 slab events using SEISAN[23]. The selected events have the following characteristics: all events are in the depth range between 50 and 310 km, travel time misfit is less than 1 second, data are well recorded at a minimum of 10 stations with azimuthal gap ≤ 270° (see Table S1 in the Supplementary Information).

For relative locations we use the program HYPODD[24] (Figure S1). We calculate differential times between P and S phases recorded at a common station for each event pair separated by ≤ 40km. This inter-event distance was interactively chosen after optimizing the linkage between the events in the first step processing of phase data in

HYPODD. Each event is strongly linked to a maximum of 10 neighboring events, having at least eight travel time observations. We used the P-wave velocity model of Dorbath et al.[25] for our starting model, and set the crustal thickness to 65 km. We used a Vp/Vs ratio of 1.75 to calculate S-wave velocities.

Three-dimensional shear wave imaging using earthquake-generated Rayleigh waves

The three-dimensional imaging of shear wave velocity structure proceeds in two steps: first we invert for Rayleigh wave phase velocities; subsequently, we invert the obtained phase velocities for shear wave velocities. We use the two-plane wave method[26] to invert for Rayleigh wave phase velocities. Observations are modeled as a sum of two interfering plane waves, each described by its amplitude, phase and backazimuth. Predicted phase and amplitude values are calculated using finite frequency sensitivity kernels[27] that incorporate the (Born) single scattering approximation[28]. Amplitudes are corrected for geometrical spreading and attenuation. We examined twelve periods in the band between 0.007 and 0.03 Hz, sensitive to Vs structure from the lower crust (~40 km depth), to the upper mantle (~200 km depth).

Data were collected from several seismic networks: PULSE (PerU Lithosphere and Slab Experiment)[11], CAUGHT (Central Andean Uplift and Geodynamics of High Topography)[12], PERUSE (Peru Slab Experiment)[13], and the global network permanent station in Lima, Peru. We picked fundamental mode Rayleigh waves for 65 well recorded teleseismic events (Figure S2a) with magnitudes ≥5.5.

We defined the study area with corners at 10°S,69°W; 18°S, 79°W; 10°S, 69°W; and 10°S, 69°W (Figure S2b). The starting velocity model (Figure S2c) accounts for different crustal thicknesses across the study area[29]. We combine the IASPEI91 velocity model for the mantle[30] and the model of James et al.[31] for the crust and use a forward algorithm[32] to predict phase velocities across the study region.

The inversion is regularized with model covariances set to 0.15 km/s. The choice of regularization parameter is based on the stability of both Rayleigh wave and shear wave inversions. Longer periods are generally less well resolved than shorter periods due to their broader sensitivity kernels. The best resolved areas are beneath the Western Cordillera, Altiplano, Eastern Cordillera, and coastal forearc and, to a lesser extent, the Sub-Andean zone (Figure S3a). The resolution within the foreland basin is mostly confined along the stations deployed in foreland basin in eastern Peru.

In the second step we invert obtained phase velocities (Figure S4) for 1D shear wave velocities[32,33]. We use the same starting model as in the previous step (Figure S2c). Sensitivity kernels for longer periods are significantly broader than shorter periods and sample greater depths. The peak sensitivities for the periods used in this study range from ~40km depth (for 33 s) up to ~200 km depth (143 s). Thus, the vertical resolution is greatest between ~40 and ~200 km, and decreases gradually with depth (below ~300 km resolution drops below 0.1, Figure S3b). The model covariance obtained for phase velocities from the two-plane wave method was used as data covariance to regularize the shear wave velocity inversion. The mean RMS misfit between predicted and observed phase velocities over all periods indicates an average error of ~0.02 km/s (Figure S3c). Results of our shear wave inversions are presented in Figure 2 and Figure S5.

Lateral and Vertical Resolution

The main new features observed in this study from the surface wave tomography include the far inboard extent of flat slab along the subducting Nazca ridge and the slab tear north of the ridge. We performed a range of tests to investigate lateral and vertical resolution to ensure the robustness of these features (see also Figures S3, S6-S10).

- Lateral Resolution

We plot the resolution matrix rows of isolated model parameters for several periods, with an emphasis on the spatial resolution at 3 locations along the northern profile north of the subducting Nazca Ridge: one where we observe re-steepening of the slab, one at the slab tear, and one along the flat slab remnant. We also investigate points at 2 locations along the subducting Nazca Ridge: one where we observe the far inboard extent of the flat slab ("long flat slab"), and one where previous studies[13] suggest the end of flat slab should be ("short flat slab"). The examination of our resolution matrix for these 5 selected nodes is primarily intended to demonstrate that we have sufficient spatial resolution to resolve the slab tear north of the ridge and the inboard extent of flat slab along the ridge. We focus on intermediate periods because they have peak sensitivity at the most relevant depths (Figure S2c). The tests show that these model parameters are able to resolve spatial scale features smaller than those discussed in this paper. The only node for which we observe a particularly broad sensitivity cone is the one at the far inboard extent of the flat slab. This suggests that, while the inboard extent of the flat slab may not be as well resolved as in other locations, a shorter flat slab would have been imaged accurately if it did exist. Our inboard extent is therefore a conservative estimate.

To demonstrate the sensitivity of our results to grid node spacing, we plot phase velocity maps for intermediate periods using 0.25° and 0.5° grid node spacing. The phase velocity maps with 0.5° grid node spacing show smoother, but consistent major features that can be observed at maps with 0.25° spacing. Further, the dispersion curves for the 5 selected nodes reflect consistency regardless of the grid node spacing. Along the northern profile in both cases we observe faster anomalies at 66 and 77 s where we observe the re-steepened slab, slow anomalies at all intermediate periods where we observe the slab tear, and fast anomalies where we observe the flat slab remnant. Along the flat slab profile we note low phase velocities at the location where previous studies suggest a resumption of the steep slab, and high phase velocities at location where we propose the end of flat slab.

We perform a series of checkerboard tests using the surface wave resolution matrices to test the size of the anomalies that can be recovered with varying periods used in this study (Figure S6). These tests show whether we have sufficient spatial resolution to recover the size of the anomaly analogous to the observed tear and whether we have sufficient resolution to resolve the inboard extent of flat slab. For this reason we plot the 5 selected nodes. In addition, these tests yield a better understanding of the spatial resolution of phase velocity maps across the study area and easily reveal areas that suffer from smearing (due to preferential ray path direction and/or lack of data). Short and intermediate periods, with peak sensitivities between 50 and 150 km depth, are able to recover smaller anomalies, equal to and smaller than the lateral extent of the observed slab tear. The tests show that we do have sufficient spatial resolution to resolve the slab tear, flat slab remnant to the east, and re-steepened slab to the west. Longer periods, which mostly sample subslab material, can recover slightly larger features. However, both shorter and longer periods are able to resolve the size of the anomaly analogous to subducting slab at the end of the flat slab. These checkerboard tests show that we are able to resolve anomalies where previous studies suggested the end of flat slab, while the node representing the far inboard extent of flat slab may be streaked due to a lack of crossing rays. Thus, based on these tests we can conclude with confidence that the inboard extent of flat slab along the subducting Nazca Ridge is not where previously assumed, but further inboard. Resolution at location representing the far inboard extent of flat slab is weak and suffers from smearing. However, our conclusion on the far inboard extent of flat slab is supported by constraints from other studies: the body wave tomography of Scire et al., [2015][34], and converted ScSp phases from Snoke, J. A., Sacks, I. S., & Okada, [1977] [35].

- Vertical Resolution

We test our vertical resolution along all profiles shown in Figure 2. Figures S7-10 show recovery tests for: the southern profile where we observe steeply dipping slab (S7); for the flat slab segment along the Nazca Ridge (S8); just north of the Nazca Ridge where we observe deepening of earthquakes and start of slab tear (S9); and the northern profile where we observe the slab tear, re-steepening of the slab and flat slab remnant (S10).

Figure S7 demonstrates our ability to recover a dipping slab south of the ridge. We model a shear wave velocity structure with a 70 km thick steeply dipping slab associated with a velocity of 4.6 km/s [S7(iv)]. This model is based on our interpretations of the observed structures that we show in Figure 2D. We predict dispersion curves for this model using the code of Saito [1980][32], add noise to predicted phase velocities, and invert them using the same starting model [S7(ii)] and regularization parameters as for model shown at S7(iii). The Gaussian noise was generated from misfits obtained in our final model using Central Limit Theorem Method and randomly assigned to predicted phase velocities. We were able to recover the steeply dipping structure, but its thickness appears greater due to vertical smearing. We were not able to recover full amplitude of the anomaly, but somewhat lower (4.45 - 4.55 km/s). Our model calculated using observed data (S7(iii)) indicates shear wave velocities above 4.55 km/s. This recovery test suggests that, in order to fully recover the amplitude of observed high shear wave velocities, the slab in S7(iv) either needs to be associated with velocities greater than 4.6 km/s, or the thickness of the slab should be greater, or both.

Figure 8 demonstrates our ability to differentiate between a flat slab with our (greater) inboard extent along the Nazca ridge track ("long flat slab") and a flat slab with shorter extent previously suggested by Cahill and Isacks [1992][13] [S8(vii)] ("short flat slab"). Plots S8(viii) and S8(ix) show recovered models. Generally, dipping structures are better resolved than flat because sensitivity kernels (Figure S2c) of several periods will penetrate longer through the structure. The tests show that we are able to recover the flat slab related high shear wave velocities. However, we observe vertical smearing, and notice that in the recovered model slab-related high velocities appear at shallower depths, resulting in high velocities in the lower crust and shallower flat slab. This is also noticeable in our model shown on S8(v). Due to vertical smearing and the gradational nature of the slab-mantle boundary in oceanic plates, the bottom of the slab is poorly resolved. Different layer discretization due to different crustal thicknesses causes the artificial undulating nature of the slab positive anomaly, also present in our model

[S8(v)]. Plots S8(viii) and S8(ix) demonstrate sufficient vertical resolution to recover the end of flat slab. We additionally plot dispersion curves at two points representing the shorter end of flat slab previously suggested by Cahill and Isacks [1992] [S8(ii)] and far inboard end [S8(iii)]. Dispersion curves predicted for shorter and longer flat slab are significantly different and the observed phase velocities match better with the longer flat slab.

Figure 9 demonstrates our ability to recover a torn slab to the north of the Nazca ridge. Figure 10 demonstrates our ability to distinguish between torn slab and a continuous slab along the northernmost profile. Figures S10(ix) and S10(x) show that lateral heterogeneities and dipping structures are well recovered (except at shallower depths where we lose resolution, see Figure S3b). Again, we are able to recover the flat slab, but with evident vertical smearing. The observed dispersion curves at locations where we observe the re-steepened slab (point 1), torn slab (point 2), and flat slab remnant (point 3) are significantly different. Shorter periods of the torn slab model at point 1 are characterized with low phase velocities, while intermediate periods have significantly higher phase velocities. In contrast, the continuous slab model is associated with high phase velocities at both short and intermediate periods. At point 2 both short and intermediate periods show low phase velocities for the torn slab model, but high phase velocities for the continuous slab model. At point 3 both short and intermediate periods are associated with high phase velocities for both torn and continuous flat slab. Generally, we are able to reproduce the observed dispersion curves with our model of torn slab (see Figure 2D), except for the low phase velocities at shorter periods at point 1. This is because we did not introduce low shear velocities in the lower crust in our starting model. Dispersion curves for the continuous flat slab differ from the observed at points 1 and 2, especially at intermediate periods that sample upper mantle material.

23. Lienert, R. B., E. Berg, L. N. Frazer, HYPOCENTER: An earthquake location method using centered, scaled, and adaptively damped least squares, Bull. Seismol. Soc. Am. 76, 771-783 (1986).
24. Waldhauser, F., W. L. Ellsworth. A Double-Difference Earthquake Location Algorithm: Method and Application to the Northern Hayward Fault, California, Bull. Seismol. Soc. Am. 90, 1353-1368 (2000).
25. Dorbath, C. Velocity structure of the Andes of central Peru from locally recorded earthquakes. *J. Geophys. Res*. **23**(2), 205-208 (1996).
26. Forsyth, D. W., and Li, A. Array analysis of two-dimensional variations in surface wave phase velocity and azimuthal anisotropy in the presence of multipathing interference. In: Levander, A. Nolet, G. (Eds), Seismic Earth: Array of broadband seismograms, *Geophysical Monograph Series* **157**, 81-98 (2005).
27. Yang, Y., Forsyth, D. W. Regional tomographic inversion of the amplitude and phase of Rayleigh waves with 2-D sensitivity kernels. Geophys. J. Int. 166, 1148-1160 (2006).
28. Zhou, Y., Dahlen, F. A., & Nolet, G. Three-dimensional sensitivity kernels for surface wave observables. *Geophys. J. Int*. **158**(1), 142-168 (2004).
29. Tassara, A., Go ̈tze, H.J., Schmidt, S. & Hackney, R., 2006. Three-dimensional density model of the Nazca plate and the Andean continental margin, J. Geophys. Res., 111, doi:10.1029/2005JB003976.

30. Kennett, B.L.N. IASPEI 1991 Seismological Tables. Bibliotech, Canberra, Australia (1991).

31. James, D. E. Andean crustal and upper mantle structure. J. Geophys. Res., 76(14), 3246-3271 (1971).

32. Saito, M. DISPER80: a subroutine package for the calculation of seismic normal mode solutions. In: Doornbos, D.J. (Ed.), Seismological Algorithms: Computational Methods and Computer Programs. Elsevier, 293–319 (1988).

33. Weeraratne, D. S., Forsyth, D. W., Fischer, K. M., & Nyblade, A. A. Evidence for an upper mantle plume beneath the Tanzanian craton from Rayleigh wave tomography. *J. Geophys. Res.*: *Solid Earth.* (1978–2012), **108**(B9) (2003).

34. Scire, A., Zandt, G., Beck. S.L., Long, M.D., Wagner, L.S., Minaya, E., Tavera, H. Imaging the transition from flat to normal subduction: Variations in the structure of the Nazca slab and upper mantle under southern Peru and northwestern Bolivia. GJI 2015 - submitted.

35. Snoke, J. A., Sacks, I. S., & Okada, H. Determination of the subducting lithosphere boundary by use of converted phases. *BSSA*, **67**(4), 1051-1060 (1977).

Figure S1 Re-located earthquakes used in this study. Colours show the depth of events (in km) and lines indicate the slab contours in 20 km depth increments. Events below 130 km are shown in black.

Figure S2 Events, grid and starting model used for the Rayleigh wave phase velocity inversions. a) Teleseismic events used in the study. b) Black diamonds represent grid nodes; blue diamonds represent corners used in the two plane wave methodology, red circles are PULSE stations, orange circles are CAUGHT stations, yellow circles are PERUSE stations and yellow star is permanent NNA station. c) Sensitivity kernels for periods used in the study with 1D starting shear wave velocity model.

Figure S3 Lateral and vertical resolution. a) Resolution for the 40 and 58 s periods. Resolution matrix diagonal for Rayleigh wave phase velocities is indicated in grey scale. Red triangles are Holocene volcanoes. Black rectangles, circles and stars are stations used in the study. b) Resolution matrix diagonal values for all 1D shear wave velocity inversions. Colours of the circles indicate average R-values for each layer. c) RMS average misfit over all periods at each point after our shear wave inversions. Colours represent the misfit in km/s. Black rectangles represent stations used in the study.

Figure S4 Calculated Rayleigh wave phase velocities for 40, 50, 58, 66, 77, and 91 s periods. Colours and contours indicate absolute phase velocities. Red triangles are Holocene volcanoes. Black rectangles, circles and stars are stations used in the study.

Figure S5 Shear wave velocity maps at 70, 95, 125, and 165 km depth. Colours represent velocity deviations with respect to the reference model (Figure S2c), while contours show absolute velocities. Green stars indicate earthquakes within 20 km depth relocated using HypoDD[24]. Red triangles represent Holocene volcanoes. Black rectangles, circles and stars are stations used in the study.

Figure S6 Checkerboard tests estimated from resolution matrix for 45, 58 and 77 s. Colours represent the recovered anomaly. Yellow stars along the northernmost profile indicate locations where we observe re-steepening of the slab, slab tear and flat slab remnant; the 2 stars along the subducting Nazca Ridge refer to locations of our (greater) inboard extent along the Nazca ridge track and a flat slab with shorter extent previously suggested by Cahill and Isacks [1992][13].

Figure S7 Recovery tests for the dipping slab south of the ridge: (i) Map showing the transect and stations locations (rectangles); (ii) starting model used in the shear wave velocity inversion; contour lines and colours are absolute shear wave velocities, black inverted triangles are stations within 35 km of the transect, red triangles are Holocene volcanoes; (iii) model calculated using observed data; (iv) model based on our interpretations of the observed structures (see also Figure 2D); (v) recovered model.

Figure S8 Recovery tests for the flat slab segment: (i) transect; (ii) dispersion curve at a location representing the shorter end of flat slab previously suggested by Cahill and Isacks [1992][13]; (iii) dispersion curve at a location representing the greater inboard extent of flat slab (proposed in this study); error bars represent one standard deviation of uncertainty; (iv) starting model; (v) model calculated using observed data; (vi) model with our (greater) inboard extent of flat slab; (vii) model with shorter flat slab previously suggested by Cahill and Isacks [1992][13]; (viii) recovered model from (vi); (ix) recovered model from (vii).

Figure S9 Recovery tests for the area just north of the Nazca Ridge where we observe a deepening of earthquakes and the southern end of the slab tear: (i) reference map; (ii) starting model; (iii) model calculated using observed data; (iv) model based on our interpretations of the torn slab (see Figure 2D); (v) recovered model.

Figure S10 Recovery tests for the northern profile where we observe the slab tear, a re-steepening of the currently subducting slab west of the tear and the flat slab remnant east of the tear: (i) transect; (ii) dispersion curve at location representing the re-steepened slab; error bars represent one standard deviation of uncertainty; (iii) dispersion curve at location representing the slab tear; (iv) dispersion curve at location representing the flat slab remnant; (v) starting model; (vi) model calculated using observed data; (vii) model with slab tear that we propose in this study; (viii) model with continuous flat slab previously suggested by Cahill and Isacks [1992][13] and other studies; (ix) recovered model from (vii); (x) recovered model from (viii). See Methods for further explanation.

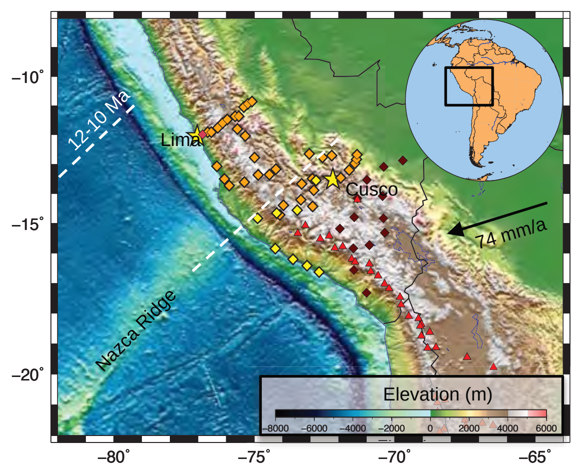

12-10 Ma
Lima
Cusco
74 mm/a
Nazca Ridge
Elevation (m)
−8000
−6000
−4000
−2000
0
2000
4000
6000
−10˚
−15˚
−20˚
−80˚
−75˚
−70˚
−65˚

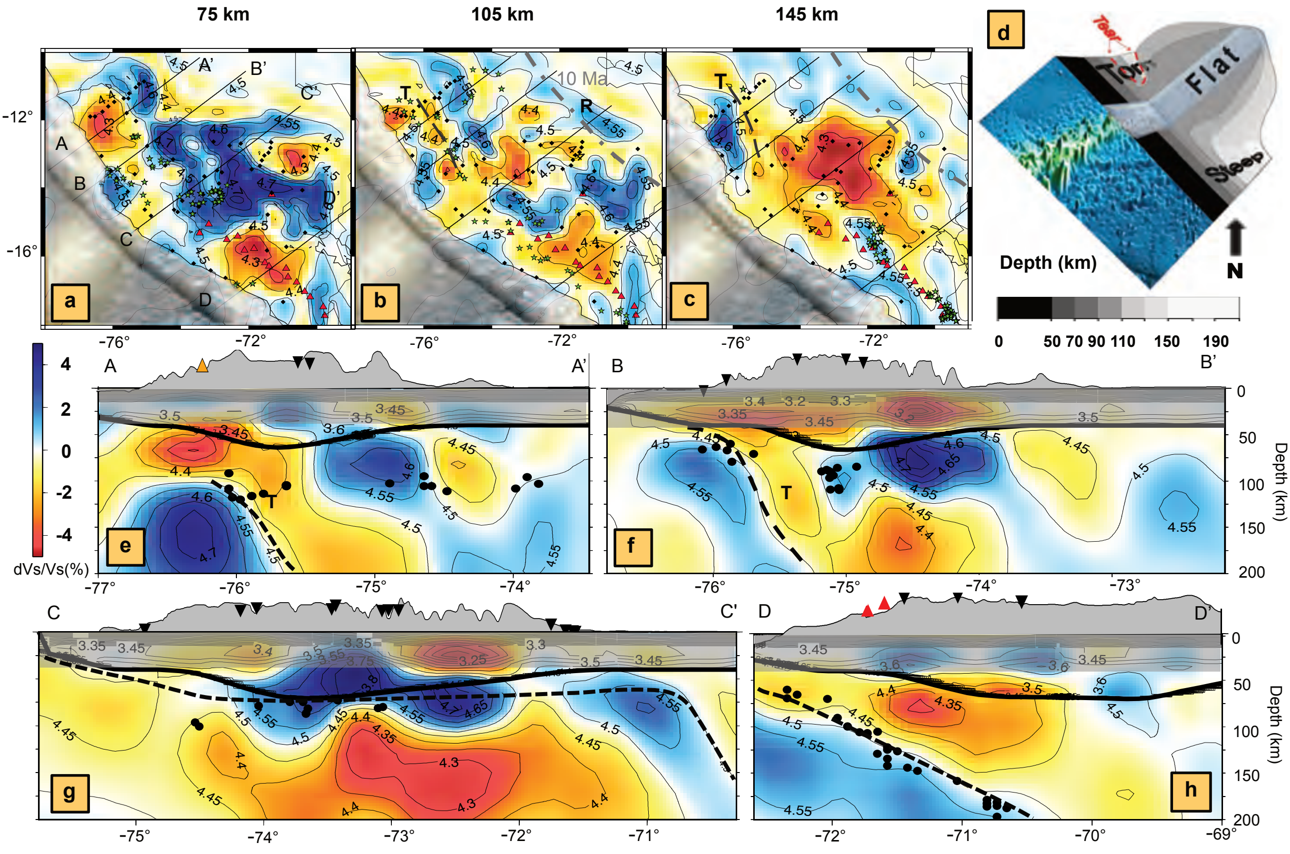

75 km
105 km
145 km
a
b
c
d
e
f
g
h
A
A'
B
B'
C
C'
D
D'
T
R
10 Ma
Tear
Torn
Flat
Steep
Depth (km)
N
0 50 70 90 110 150 190
dVs/Vs(%)
Depth (km)
-12°
-16°
-76°
-72°

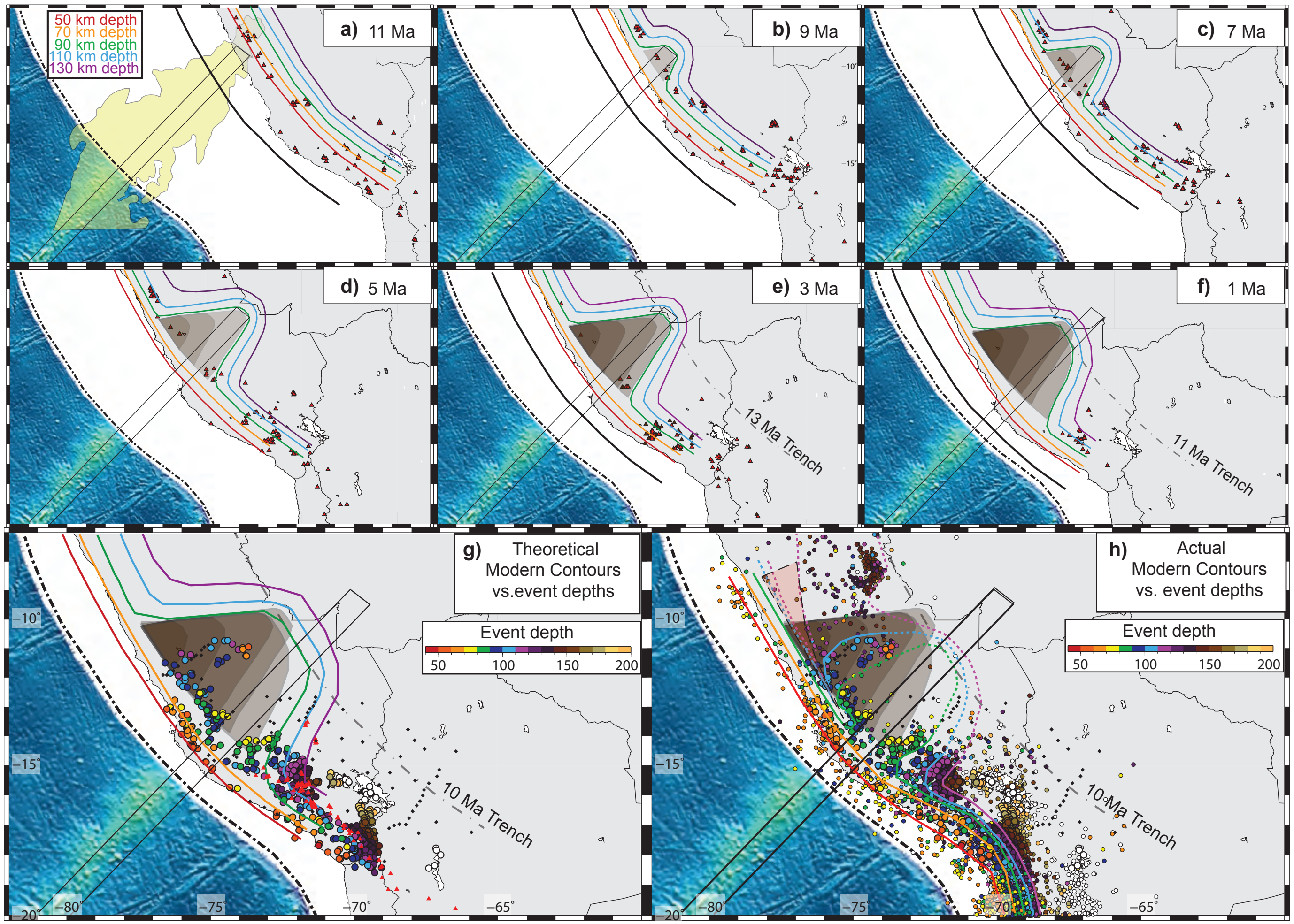

50 km depth
70 km depth
90 km depth
110 km depth
130 km depth
a) 11 Ma
b) 9 Ma
c) 7 Ma
d) 5 Ma
e) 3 Ma
f) 1 Ma
13 Ma Trench
11 Ma Trench
g) Theoretical Modern Contours vs.event depths
h) Actual Modern Contours vs. event depths
Event depth
50 100 150 200
10 Ma Trench
−10°
−15°
−20°
−80°
−75°
−70°
−65°